energies

MDPI

Article

Thermodynamic Investigation and Economic Evaluation of a High-Temperature Triple Organic Rankine Cycle System

Pengcheng Li [1,2], Chengxing Shu [1], Jing Li [3,*], Yandong Wang [4], Yanxin Chen [1], Xiao Ren [5], Desuan Jie [1] and Xunfen Liu [1]

[1] School of Automotive and Transportation Engineering, Hefei University of Technology, 193 Tunxi Road, Hefei 230002, China; lpc1988@hfut.edu.cn (P.L.); 2023171652@mail.hfut.edu.cn (C.S.); 2021212903@mail.hfut.edu.cn (Y.C.); jieds@126.com (D.J.); jindidaili@126.com (X.L.)
[2] Dongfang Boiler Co., Ltd., Dongfang Electric Group, Zigong 643001, China
[3] Research Center for Sustainable Energy Technologies, Energy and Environment Institute, University of Hull, Hull HU6 7RX, UK
[4] Hefei General Machinery Research Institute, 888 Changjiang Road, Hefei 230031, China; can0101@163.com
[5] School of New Energy, China University of Petroleum, Qingdao 266580, China; renxiao@upc.edu.cn
* Correspondence: jing.li@hull.ac.uk

Abstract: Triple organic Rankine cycle (TORC) is gradually gaining interest, but the maximum thermal efficiencies (around 30%) are restricted by low critical temperatures of common working fluids (<320 °C). This paper proposes a high-temperature (up to 400 °C) TORC system to ramp up efficiency. A near-azeotropic mixture biphenyl/diphenyl oxide (BDO), which has a stellar track record in the high-temperature ORC applications, is innovatively adopted as the top and middle ORC fluid simultaneously. Four conventional organic fluids are chosen for the bottom ORC. A mixing heat exchanger connects the top and middle ORCs to reduce irreversible loss. Thermodynamic analysis hints that the optimal performance is achieved on the use of benzene as the bottom fluid. The maximum thermal and exergy efficiencies are respectively 40.86% and 74.14%. The largest exergy destruction occurs inside the heat exchanger coupling the middle and bottom ORCs, accounting for above 30% of the total entropy generation. The levelized energy cost (LEC) is 0.0368 USD/kWh. Given the same heat source condition, the TORC system can boost the efficiency by 1.02% and drive down LEC by 0.0032 USD/kWh compared with a BDO mixture-based cascade ORC. The proposed system is promising in solar thermal power generation and Carnot battery applications using phase change materials for storage.

Keywords: triple organic rankine cycle; biphenyl/diphenyl oxide; thermal efficiency; exergy efficiency; levelized energy cost

Citation: Li, P.; Shu, C.; Li, J.; Wang, Y.; Chen, Y.; Ren, X.; Jie, D.; Liu, X. Thermodynamic Investigation and Economic Evaluation of a High-Temperature Triple Organic Rankine Cycle System. *Energies* **2023**, *16*, 7818. https://doi.org/10.3390/en16237818

Academic Editor: Juan Carlos Ramos

Received: 31 October 2023
Revised: 20 November 2023
Accepted: 24 November 2023
Published: 28 November 2023

1. Introduction

Organic Rankine cycle (ORC) technology is a well-grounded and promising way to convert heat into power. It is one of the leading ways to achieve pumped thermal electricity storage in Carnot battery technology [1]. For high-temperature heat sources, cascade or even triple organic Rankine cycle (TORC) is commonly adopted to extract the exergy more adequately and realize stage-wise utilization of the energy. TORC technology is booming and attracting increasingly widespread attention. Prabhu et al. compared the performance of 10 MWe parabolic trough power stations with different structures. The highest net efficiency of 27.5% was achieved for a TORC arrangement when the top cycle evaporation temperature was 318 °C and the degree of superheat was around 60 °C. Toluene, cyclohexane and butane were the top, middle and bottom cycle fluids, respectively. TORC is inferior to the most efficient cascade cycles due to the additional internal losses, complexity and cost [2]. Mahmoud et al. devised an independent TORC system adopting three hydrocarbons as the working fluids to recover waste heat from comprehensive

crude oil refining and aromatics facilities with a maximum temperature of 160 °C [3]. Zhang et al. researched both TORC and four-stage ORC systems. For a single-phase heat source of 300 °C hot air, the highest thermal efficiencies of 26.86% and 26.22%, exergy efficiencies of 79.46% and 77.56%, and levelized energy costs (LECs) of 0.063 USD/kWh and 0.072 USD/kWh could be achieved by the two systems. For a two-phase heat source of 185 °C saturated steam, the highest thermal efficiencies of 23.64% and 24.43%, exergy efficiencies of 69.94% and 72.26%, and LECs of 0.069 USD/kWh and 0.068 USD/kWh could be obtained [4]. Yu et al. conducted analysis on an R245fa-based TORC system. When the geothermal fluid temperature was 200 °C, the net power output was 3.8% and 2.4% higher than that of the single-stage and cascade cycles, respectively. The LEC of the TORC was approximately 0.04 USD/kWh [5].

Alongside this, TORC configuration is also applied in the field of recovering the cold exergy of liquefied natural gas (LNG). García et al. investigated a TORC system with LNG and industrial waste heat as the cold and heat sources. The working fluid of each stage is argon, methane, and R14. The highest exergy efficiency was 85.6% [6]. Zhang et al. found that when the waste heat temperature was above 100 °C, the TORC system had higher net power output and thermal efficiency than those of the single-stage one. The optimal thermal and exergy efficiencies were respectively 32.5% and 39.08% at the heat source temperature of 150 °C [7]. Han et al. simulated a TORC system using LNG and 127.17 °C waste heat from ship as the cold and heat sources. The highest efficiencies were 31.72%, 19.86% and 27.53% for the top, middle, and bottom ORCs using the working fluids of R290, R601a, and R236ea, respectively. The cost of each cycle was 0.71, 1.33 and 0.98 million USD/year [8].

Notably, the maximum evaporation temperatures of the above TORC systems are limited to below 320 °C due to the low critical temperatures of the conventional refrigerants, hydrocarbons, and siloxanes [9]. A biphenyl/diphenyl oxide (BDO) mixture has significant potential for high- or medium-temperature ORC applications [10] and has been reported extensively in the literature. The mixture consists of 73.5% diphenyl oxide and 26.5% biphenyl and possesses extraordinarily low viscosity and high stability in a large temperature interval from 12 °C to 400 °C [11,12]. Bronicki successfully tested a cascade cycle device employing the BDO mixture and monochlorobenzene as the first- and second-stage cycle fluids. The overall efficiency was 8.5% and the power output was 680 W at the first-stage cycle evaporation temperature of 195 °C [13]. Bombarda et al. employed the BDO mixture as the bottom cycle fluid in a binary liquid metal-ORC distributed system. An efficiency of 46% was claimed [14]. Vescovo briefly introduced the application of BDO mixture in high-temperature ORC. The described system efficiency ranged from 30% to 34% [15,16]. Sampedro et al. presented a toluene ORC topped by a wet-to-dry cycle using the BDO mixture. The maximal power output by the cascade cycle was 96 kW at the heat source temperature of 492 °C [17]. Li et al. innovatively adopted the BDO mixture as the heat transfer, storage, and power cycle fluid in a cascade organic-steam Rankine cycle system [18,19]. The thermal efficiency was 42.90% when the BDO was vaporized at 390 °C [19]. Ren et al. put forward a cascade ORC topped by a BDO mixture cycle. The maximum thermal efficiency was 40.26% irrespective of pressure drop in all the heat exchangers [20]. Li et al. analyzed a novel partial cascade organic-steam Rankine cycle utilizing the BDO mixture as the ORC fluid. The maximum efficiency was 45.3% when the ORC and water evaporation temperatures were 400 °C and 290 °C, respectively [21].

In order to ramp up the maximum evaporation temperature and the heat-to-power conversion efficiency of existing TORCs, this paper proposes a BDO mixture-based TORC system. The novelty and contribution include: (a) the BDO mixture is applied in a TORC system for the first time, although its potential in cascade ORCs has been explored; (b) the maximum evaporation temperature of the TORC reaches 400 °C in view of BDO's high stability, which is appreciably higher than those of 320 °C achieved by conventional TORCs; (c) thermodynamic and economic comparisons with a BDO mixture-based cascade ORC is conducted.

More precisely, the BDO mixture is simultaneously adopted as the top and middle ORC working fluid, and conventional organic fluids for the bottom ORC. The above experimental and simulation studies on the BDO mixture [10–21] set the stage for its application in high temperature TORC. The BDO mixture in the top cycle evaporates at 400 °C and drives the top turbine. Both the top and middle ORCs are equipped with an internal recuperator to recover the exergy in the exhaust vapor at the turbine outlets. The superheated vapor at the recuperators' outlets serves as the heat source for the next-stage cycle. A mixing heat exchanger (MHX) connects the top and middle ORCs to reduce the irreversible loss in heat transfer.

The operating philosophy and characteristics of the TORC are elaborated, and mathematical models are built. Thermal and exergy efficiencies of the TORC were investigated with respect to the MHX outlet temperature, middle ORC condensation temperature, and different bottom ORC fluids, followed by the evaluation of the entropy generation in each component and the economic index. Finally, a comprehensive comparison with a BDO mixture-based cascade ORC is carried out. The structure of the work is visualized in Figure 1.

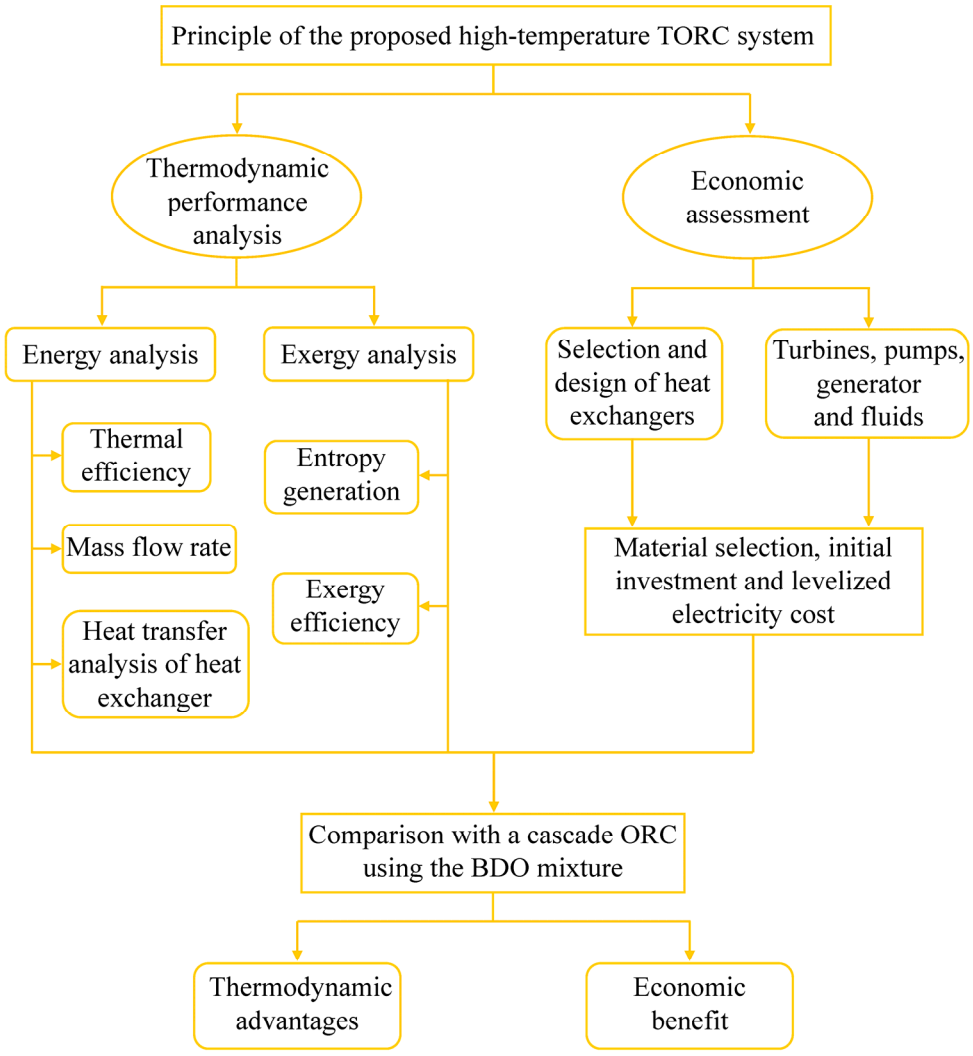

Figure 1. Overview of the work.

2. System Description

Figure 2 shows the schematic diagram of the proposed high-temperature TORC system. The heat source can be waste heat in industrial production, exhaust heat from land

or marine engines, geothermy, biomass combustion, concentrating solar heat, etc. The cold source can be ambient temperature air or water.

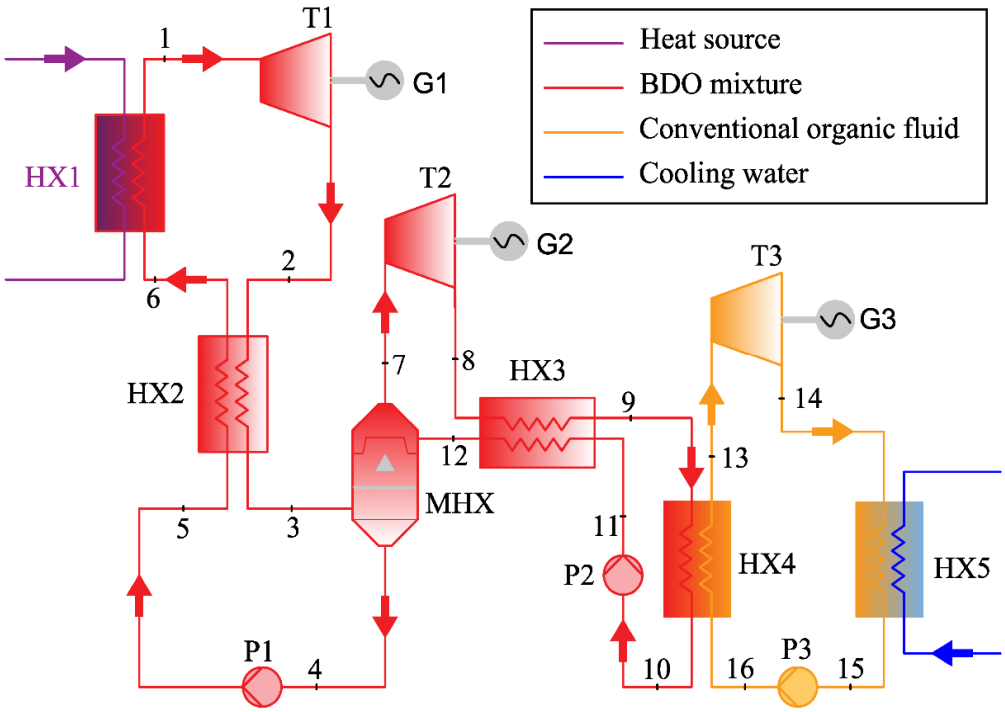

Figure 2. Schematic diagram of the TORC.

The system consists of three loops: top ORC in red, middle ORC in red, and bottom ORC in orange. The top and middle cycles are coupled by an MHX. MHXs are open-type direct contact heat exchangers (HXs) where one type or different fluid streams exchange heat and mix with each other [22]. Indirect heat exchange between the two cycles is thus avoided, leading to enhanced heat transfer performance and reduced cost of equipment [23]. The function of an MHX is similar to that of the absorbers in absorption refrigeration and the jet HXs in jet refrigeration. MHXs are widely applied in fuel cells to ensure adequate mixing of the fuels with oxidant (usually air) and rapid evaporation [24]. MHXs are divided into four types according to the structural characteristics: liquid film, liquid column, packed, and jet type. The liquid film type is exemplified in Figure 2. The subcooled liquid of the middle cycle flows into the MHX, and is sprayed to form liquid film after encountering an obstacle. Meanwhile, the superheated vapor of the top cycle flows into the bottom of MHX and is mixed with the liquid film. Due to gravity, the top and bottom outlets of MHX are respectively saturated vapor and saturated liquid after sufficient heat exchange in the middle of MHX. The former drives the turbine 2 (T2) and the latter flows into the pump 1 (P1). Notably, the outlet temperatures and pressures of MHX are correspondingly the same ($T_4 = T_7$ and $p_4 = p_7$).

After being pressurized, the subcooled BDO mixture from P1 outlet is heated in HX2 by the exhaust vapor from T1, and further heated to saturated vapor in HX1 to drive T1. After outputting technical work and generating electricity, the exhaust vapor in superheated state is precooled in HX2 and enters the MHX. Heat and mass transfer occurs between the superheated vapor from the top cycle and the subcooled liquid from the middle cycle in the MHX. The MHX serves as the condenser of the top cycle and the evaporator of the middle cycle concurrently. HX2 and HX3 are respectively the internal recuperators of the two cycles. The operating principles of the middle ORC are the same as those of the top ORC. In the bottom ORC, conventional fluids such as benzene, cyclohexane, R141b and pentane can be adopted. The middle ORC is coupled with the bottom ORC through HX4, which acts as the condenser of the former and the evaporator of the latter simultaneously.

The exhaust superheated vapor from the bottom ORC turbine enters HX5, and is cooled to saturated liquid by water at ambient temperature.

3. Mathematical Models

3.1. Thermodynamic Models

Subcritical cycles are considered for the TORC. Figure 3 illustrates the T-s diagram.

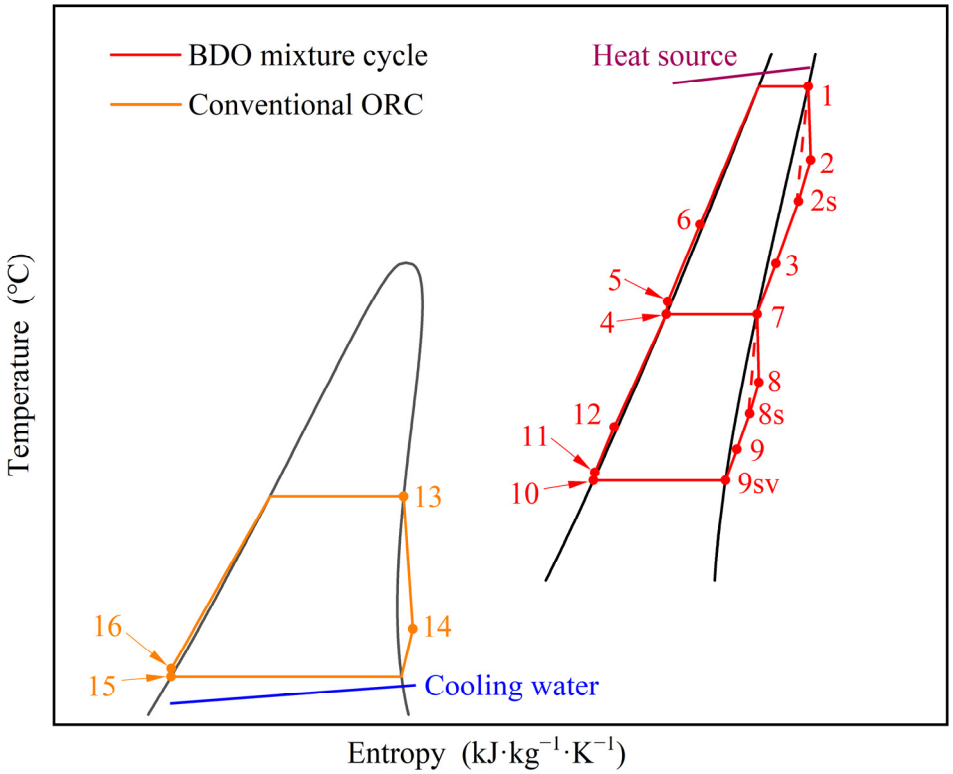

Figure 3. *T-s* diagram of the TORC.

3.1.1. Turbines

The work produced by $T1$, $T2$, and $T3$ can be derived as follows:

$$W_{T1} = m_{top} \cdot (h_1 - h_2) = m_{top} \cdot (h_1 - h_{2s}) \cdot \varepsilon_T \quad (1)$$

$$W_{T2} = m_{mid} \cdot (h_7 - h_8) = m_{mid} \cdot (h_7 - h_{8s}) \cdot \varepsilon_T \quad (2)$$

$$W_{T3} = m_{bot} \cdot (h_{13} - h_{14}) = m_{bot} \cdot (h_{13} - h_{14s}) \cdot \varepsilon_T \quad (3)$$

where the subscript "s" indicates isentropic, and m_{top}, m_{mid} and m_{bot} are the mass flow rates of the top, middle, and bottom ORCs (kg/s). ε_T is the turbine efficiency.

3.1.2. Heat Exchangers

The heat balance in $HX2$, $HX3$, and $HX4$ is described by:

$$m_{top} \cdot (h_2 - h_3) = m_{top} \cdot (h_6 - h_5) \quad (4)$$

$$m_{mid} \cdot (h_8 - h_9) = m_{mid} \cdot (h_{12} - h_{11}) \quad (5)$$

$$m_{mid} \cdot (h_9 - h_{10}) = m_{bot} \cdot (h_{13} - h_{16}) \quad (6)$$

The efficiencies of $HX2$ and $HX3$ are determined as [19]:

$$\varepsilon_{HX2} = \frac{h_6 - h_5}{h_2 - h_{3sv}} = \varepsilon_{HX3} = \frac{h_{12} - h_{11}}{h_8 - h_{9sv}} \tag{7}$$

Since there exists multiple HXs, taking into account the negative effects of pressure drop makes the performance results more reasonable. Table 1 provides the recommended allowable pressure loss under different operating conditions.

Table 1. Allowable pressure drop [25].

Intel Pressure (kpa)	<100	100–170	170–1100	1100–3100	3100–8100
Allowable pressure drop (kpa)	p/10	5–35	35	35–180	70–500

3.1.3. Pumps

The work consumed by $P1$, $P2$, and $P3$ are given by:

$$W_{P1} = m_{top} \cdot (h_5 - h_4) = m_{top} \cdot (h_{5s} - h_4)/\varepsilon_P \tag{8}$$

$$W_{P2} = m_{mid} \cdot (h_{11} - h_{10}) = m_{mid} \cdot (h_{11s} - h_{10})/\varepsilon_P \tag{9}$$

$$W_{P3} = m_{bot} \cdot (h_{16} - h_{15}) = m_{mid} \cdot (h_{16s} - h_{15})/\varepsilon_P \tag{10}$$

where ε_P is the pump efficiency.

3.1.4. Saturated Entropies of the BDO

The saturation state parameters of the BDO mixture (such as T, p, h, v, ρ, c_p, etc.) at intervals of 10 °C can be obtained from a supplier Eastman Corp [26]. The saturated parameters at other temperatures can be calculated by linear interpolation.

The specific entropy in a saturated state can be deduced by [27]:

$$\mathrm{d}h = T\mathrm{d}s + v\mathrm{d}p \tag{11}$$

3.1.5. Superheated Enthalpies of the BDO

The BDO mixture at both T1 and T2 outlets are in superheated state, and the enthalpies h_2 and h_8 cannot be derived directly. To tackle this problem, an equivalent hot side temperature (T_{EHST})-based ORC efficiency model was developed [28], in which only the saturated parameters were required. For the middle ORC:

$$T_{EHST} \approx \frac{h_7 - h_{10} - v_{10}(p_7 - p_{10})}{s_7 - s_{10}} \tag{12}$$

The efficiency of ORC in a basic structure ($\eta_{ORC,b}$) without an internal heat exchanger can be established with the assistance of T_{EHST} [26].

$$\eta_{ORC,\,b} = \left(1 - \frac{T_{10}}{T_{EHST}}\right) \cdot \frac{\varepsilon_T \cdot \varepsilon_G + v_{10} \cdot (p_7 - p_{10}) / \left(\varepsilon_P \cdot \int_7^{9sv} v_{sv} dp\right)}{1 + v_{10} \cdot (p_7 - p_{10}) / \left(\int_7^{9sv} v_{sv} dp\right)} \tag{13}$$

where ε_G is the generator efficiency. $\int_7^{9sv} v_{sv} dp$ can be obtained according to the composite trapezoidal rule.

According to the original definition of efficiency, $\eta_{ORC,\,b}$ can also be expressed as [21]:

$$\eta_{ORC,\,b} = \frac{(h_7 - h_8) \cdot \varepsilon_G - (h_{11} - h_{10})}{h_7 - h_{11}} \tag{14}$$

h_8 can then be deduced, and the same is true for h_2.

Most ORC fluids in liquid state are incompressible, and most of the heat is taken away during the condensation process [28]. h_{11s} can thus be calculated by

$$h_{11s} \approx h_{10} + v_{10} \cdot (p_{11s} - p_{10}) \tag{15}$$

3.1.6. Thermal Efficiency

The thermal efficiencies of the top, middle, and bottom ORCs are:

$$\eta_{th,\ top} = \frac{W_{net,top}}{Q_{top}} = \frac{W_{T1} \cdot \varepsilon_G - W_{P1}}{m_{top} \cdot (h_1 - h_6)} \tag{16}$$

$$\eta_{th,\ mid} = \frac{W_{net,mid}}{Q_{mid}} = \frac{W_{T2} \cdot \varepsilon_G - W_{P2}}{m_{mid} \cdot (h_7 - h_{12})} \tag{17}$$

$$\eta_{th,\ bot} = \frac{W_{net,bot}}{Q_{bot}} = \frac{W_{T3} \cdot \varepsilon_G - W_{P3}}{m_{bot} \cdot (h_{13} - h_{16})} \tag{18}$$

where Q is the absorbed heat, W_{net} is the net power output, and ε_G is the generator efficiency.

The thermal efficiency of the TORC can be appraised by:

$$\eta_{th,\ TORC} = \frac{W_{net,TORC}}{Q_{top}} = \frac{(W_{T1} + W_{T2} + W_{T3}) \cdot \varepsilon_G - W_{P1} - W_{P2} - W_{P3}}{m_{top} \cdot (h_1 - h_6)} \tag{19}$$

3.1.7. Entropy Generation

The entropy generation represents the thermodynamic irreversibility in the components. The equations are listed in Table 2 [23].

Table 2. Definition of the entropy generation in different components.

Equipment	Equation
T1	$\Delta S_{T1} = m_{top} \cdot (s_2 - s_1)$
T2	$\Delta S_{T2} = m_{mid} \cdot (s_8 - s_7)$
T3	$\Delta S_{T3} = m_{bot} \cdot (s_{14} - s_{13})$
HX1	$\Delta S_{HX1} = m_{top} \cdot \left(s_1 - s_6 - \frac{h_1 - h_6}{T_1 + 10}\right)$
HX2	$\Delta S_{HX2} = m_{top} \cdot (s_6 - s_5 + s_3 - s_2)$
HX3	$\Delta S_{HX3} = m_{mid} \cdot (s_{12} - s_{11} + s_9 - s_8)$
HX4	$\Delta S_{HX4} = m_{mid} \cdot (s_{10} - s_9) + m_{bot} \cdot (s_{13} - s_{16})$
HX5	$\Delta S_{HX5} = m_{bot} \cdot \left(s_{15} - s_{14} - \frac{h_{15} - h_{14}}{T_{15}}\right)$
MHX	$\Delta S_{MHX} = m_{top} \cdot (s_4 - s_3) + m_{mid} \cdot (s_7 - s_{12})$
P1	$\Delta S_{P1} = m_{top} \cdot (s_5 - s_4)$
P2	$\Delta S_{P2} = m_{mid} \cdot (s_{11} - s_{10})$
P3	$\Delta S_{P3} = m_{bot} \cdot (s_{16} - s_{15})$

3.1.8. Exergy Efficiency

The exergy absorbed by the top, middle, and bottom ORCs are estimated as [21]:

$$Ex_{top} = m_{top} \left[h_1 - h_6 - T_a(s_1 - s_6)\right] \tag{20}$$

$$Ex_{mid} = m_{mid} \left[h_7 - h_{12} - T_a(s_7 - s_{12})\right] \tag{21}$$

$$Ex_{bot} = m_{bot} \left[h_{13} - h_{16} - T_a(s_{13} - s_{16})\right] \tag{22}$$

where T_a is the ambient temperature (°C).

The exergy efficiencies of the top, middle, bottom ORCs and TORC can be appraised by [4]:

$$\eta_{ex,\ top} = \frac{W_{net,top}}{Ex_{top}} \tag{23}$$

$$\eta_{ex,\ mid} = \frac{W_{net,mid}}{Ex_{mid}} \tag{24}$$

$$\eta_{ex,\ bot} = \frac{W_{net,bot}}{Ex_{bot}} \tag{25}$$

$$\eta_{ex,\ TORC} = \frac{W_{net,\ \ TORC}}{Ex_{top}} \tag{26}$$

3.2. Economic Models

3.2.1. Cost of Equipment

The purchased cost of a *HX* is [21,29]:

$$C_{HX} = 3.28 \times 10^4 \times \left(\frac{A}{80}\right)^{0.68} \cdot F_M \cdot F_P \cdot F_T \tag{27}$$

where A is the *HX* area (m2). F_M, F_P, and F_T are the material factor, pressure factor, and temperature factor.

The cost of a turbine is [30,31]:

$$C_T = 6000 \cdot (W_T)^{0.7} \cdot F_M \cdot F_P \cdot F_T \tag{28}$$

The cost of a generator is [32,33]:

$$C_G = 60 \cdot (\varepsilon_G \cdot W_T)^{0.95} \tag{29}$$

The purchased cost of a pump is [34,35]:

$$log_{10} C_P = K_1 + K_2 log_{10} W + K_3 (log_{10} W)^2 \tag{30}$$

where C_P is the basic cost of the equipment assuming ambient operating pressure and carbon steel construction in the year of 2001.

When taking the specific material of equipment and operating pressure into account, the bare module cost for a pump should be corrected as [34,35]:

$$C_{BM,\ P} = C_P \cdot (B_1 + B_2 \cdot F_M \cdot F_p) \tag{31}$$

where F_p is the pressure correction factor of a pump and it is determined by [34,35]:

$$log_{10} F_p = C_1 + C_2 log_{10}(0.01p - 1) + C_3 \left[log_{10}(0.01p - 1)\right]^2 \tag{32}$$

K_1, K_2, K_3, B_1, B_2, C_1, C_2, and C_3 are the fitting cost coefficients, and the values are indexed in Table 3 [29,30]. Since the unit in the two parentheses of Equation (32) is the gage pressure in bar, thus a transformation from kPa to bar is needed to fit the equation.

Table 3. Values of constants for the pumps.

K_1	K_2	K_3	B_1	B_2	C_1	C_2	C_3	F_M	F_p
3.4771	0.135	0.1438	1.89	1.35	−0.3935	0.3957	−0.00226	1.6	1

3.2.2. Cost of Fluids

The cost of BDO mixture (C_{BDO}) and the cost of bottom ORC fluid ($C_{bot,\ fluid}$) can be respectively appraised by

$$C_{BDO} = P_{BDO} \cdot M_{BDO} \tag{33}$$

$$C_{bot,\ fluid} = P_{bot,\ fluid} \cdot M_{bot,\ fluid} \tag{34}$$

where P_{BDO} and $P_{bot,\ fluid}$ are the prices of BDO mixture and bottom fluid. M_{BDO} and $M_{bot,\ fluid}$ represent their filling mass.

However, accurately evaluating the filling mass of an ORC system is not easy because of the rare report on this aspect. The charging weight is 5.57 kg and 5.4 kg for a 1-kWe net electricity generation in the light of Refs. [36,37]. Pursuant to this data, M_{BDO} and $M_{bot,\ fluid}$ are proportional to $(W_{top} + W_{mid}) \cdot \varepsilon_G$ and $W_{bot} \cdot \varepsilon_G$, respectively.

3.2.3. Levelized Energy Cost

The total capital cost (C_{tot}) is determined by the cost of working fluid and main equipment, including HXs, turbines, pumps, and generators. The investment in MHX can be ignored as it has a significantly lower cost than other components [21,38]. Determining C_{tot} is reasonable by

$$C_{tot} = C_{\ HX} + C_T + C_{BM,P} + C_G + C_{BDO} + C_{bot,\ fluid} \tag{35}$$

The actual cost needs to be converted from the cost of 2001 by calculating the Chemical Engineering Plant Cost Index (*CEPCI*) [34,39]. The cost of 2023 should be corrected as

$$C_{tot,\ 2023} = C_{tot,\ 2001} \cdot CEPCI_{2023} / CEPCI_{2001} \tag{36}$$

Capital recovery factor (*CRF*) is calculated by [34,35]

$$CRF = \frac{i \cdot (1+i)^{LT}}{(1+i)^{LT} - 1} \tag{37}$$

where i is the annual loan interest rate, and LT is the system lifetime.

LEC is the ratio of expenditure to revenue, and can be deduced by [34,40]

$$LEC = \frac{CRF \cdot C_{tot} + C_{OM}}{t_{op} \cdot W_{net}} \tag{38}$$

where t_{op} is the operation time (h), and C_{OM} is the operation and maintenance cost, which is 1.5% of C_{tot} [34,35].

4. Results and Discussion

Table 4 displays the design parameters. Given the top ORC evaporation temperature (T_1) and bottom ORC condensation temperature (T_{15}), the middle ORC evaporation and condensation temperatures (T_7 and T_{10}) emerge as crucial parameters because they not only affect each subcycle efficiency, but also influence the TORC efficiency. As T_7 equals to the top ORC condensation temperature, i.e., MHX outlet temperature (T_4), T_4 and T_{10} are taken as variables in this simulation. The parameters for the rest state points can be determined by conditions such as conservation of energy, pump, and turbine efficiencies, and heat transfer temperature difference.

Table 4. Specific parameters for calculation.

Parameters	Design Value
Net power output of TORC system [21,41], $W_{net,\ TORC}$	10 MW
ORC turbine efficiency [19,32], ε_T	0.85
Pump efficiency [42,43], ε_P	0.8
Generator efficiency [30,34], ε_G	0.95
Efficiencies of HX2 and HX3 [30,35], $\varepsilon_{HX2} = \varepsilon_{HX3}$	0.7
Minimum heat transfer temperature difference [19,20], ΔT_{min}	10 °C
Evaporation temperature of the top ORC [21], T_1	400 °C
Condensation temperature of the bottom ORC [20], T_{15}	30 °C
Ambient temperature [21,44], T_a	15 °C
CEPCI in 2001 [22], $CEPCI_{2001}$	397
CEPCI in 2023 [45], $CEPCI_{2023}$	808.9
Interest rate [35], i	5%
Annual operating time [5,46], t_{op}	7000 h
System lifetime [34,35], LT	20 years

The ranges of T_4 and T_{10} are determined in the following considerations. First, maintaining a vacuum below 5 kPa in the HXs is a technical limit [47,48]. As 5 kPa corresponds to the saturation temperature of 153 °C for the BDO mixture, the lower limit of T_{10} is chosen as 153 °C. Second, limited by the minimum heat transfer temperature difference (ΔT_{min}), $T_4 \geq T_{10} + \Delta T_{min}$. The lower limit of T_4 is selected as 163 °C. Third, the upper limit of T_{10} is taken as the critical temperature of each bottom ORC fluid plus ΔT_{min} in HX4. Forth, as $T_1 \geq T_4 + \Delta T_{min}$ in the top ORC, the upper limit of T_4 is set as 390 °C.

4.1. Thermodynamic Performance Analysis

4.1.1. Thermal Efficiency

Figure 4 exhibits the variation of $\eta_{th,\ TORC}$ with T_4 and T_{10} in the circumstance of considering pressure drop. The actual pressure drop is taken as the minimum allowable pressure drop in Table 1. The size of each curved surface varies because the different critical temperatures of bottom ORC fluids limit the maximum T_{10}. Each surface becomes narrower as T_{10} increases. The reason is that as $T_4 \geq T_{10} + \Delta T_{min}$, the lower limit of T_4 rises as T_{10} ascends, while the upper limit of T_4 is maintained at 390 °C. For example, T_4 ranges from 170 °C to 390 °C when T_{10} is 160 °C, while T_4 varies from 310 °C to 390 °C when T_{10} is 300 °C for benzene or cyclohexane. Given T_4, $\eta_{th,\ TORC}$ decreases monotonously with the increment in T_{10}. The optimum $\eta_{th,\ TORC}$ is achieved at the lowest T_{10} of 153 °C for the four bottom fluids.

Figure 5 displays the cross section corresponding to T_{10} of 153 °C. $\eta_{th,\ TORC}$ first increases and then decreases with T_4. The peak value of each curve is obtained when T_4 is 257 °C. The maximum $\eta_{th,\ TORC}$ is 40.86% when benzene is employed, and it is noticeably higher than that of the results obtained by all the previous TORC studies [2,4,7,8,21,22]. Table 5 summarizes the thermodynamic parameters of each state point for benzene at the optimum condition. The pressure drop of the cold side in HX1, HX2, and HX4 is postulated to be 35 kPa, and it is 5 kPa for HX3. Whereas it is 5 kPa, 0.633 kPa, 0.57 kPa, and 1.76 kPa on the hot side of HX2, HX3, HX4, and HX5, respectively.

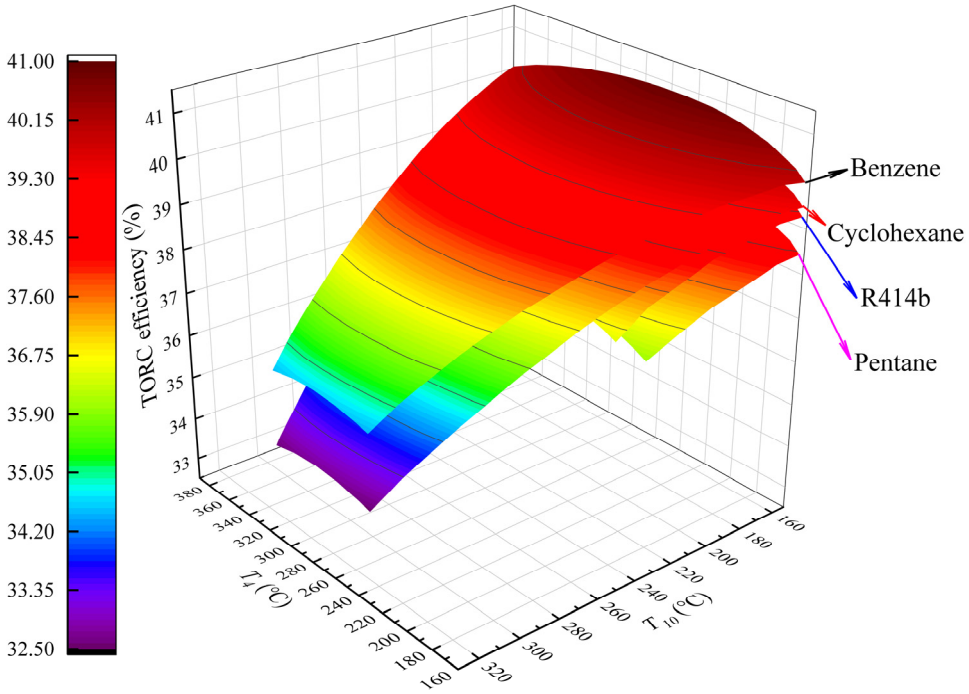

Figure 4. Variations of TORC thermal efficiency with T_4 and T_{10}.

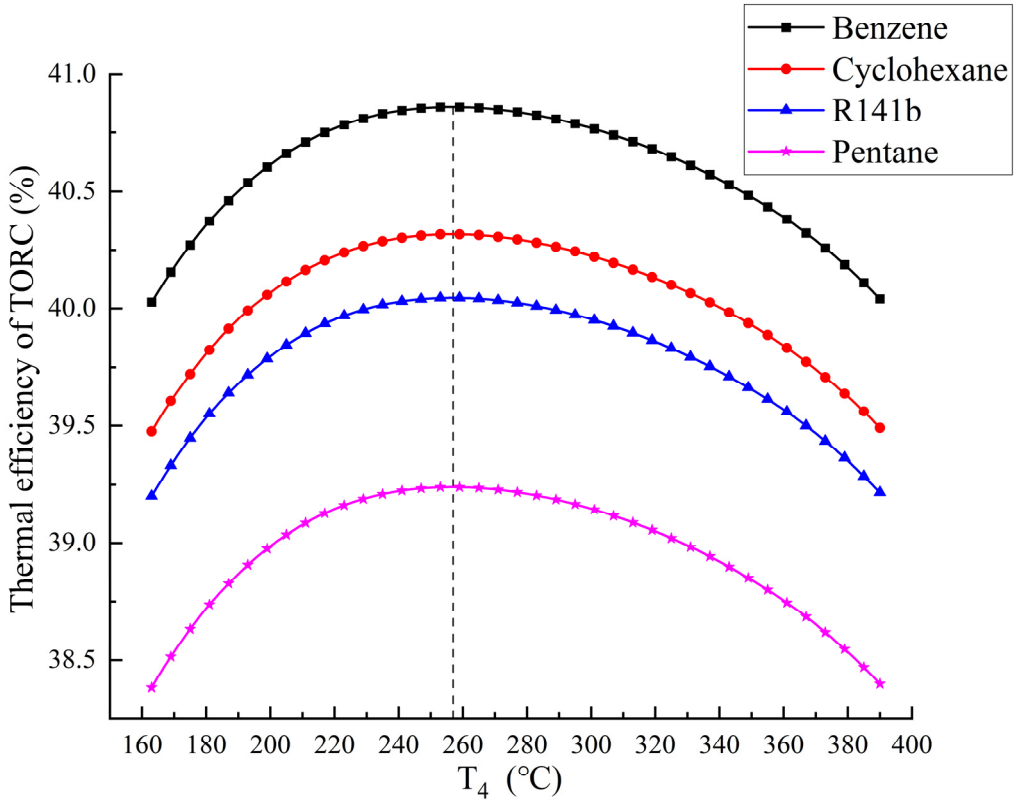

Figure 5. Variations of TORC thermal efficiency with T_4 when $T_{10} = 153$ °C.

Figures 6 and 7 present the variations of subcycle net power outputs and efficiencies on the use of benzene at T_{10} of 153 °C. The net power output for the top ORC drops linearly as T_4 rises, while it increases linearly for the middle ORC and stays almost stable for the bottom ORC. Similarly, the top ORC efficiency ($\eta_{th,\,top}$) decreases linearly, the middle

ORC efficiency ($\eta_{th,\ mid}$) increases approximately linearly, and the bottom ORC efficiency ($\eta_{th,\ bot}$) remains constant with T_4. The reason is that given T_1, T_{15}, and T_{10}, the temperature difference between the top ORC declines, while it increases for the middle ORC and remains unchanged for the bottom ORC. As the optimal T_4 and T_{10} are fixed for different bottom ORC fluids, $\eta_{th,\ top}$ of 16.22% and $\eta_{th,\ mid}$ of 14.71% can be calculated at the optimal condition. However, $\eta_{th,\ bot}$ varies depending on the bottom fluids, leading to a difference in $\eta_{th,\ TORC}$. The minimum $\eta_{th,\ bot}$ is 15.45% for pentane and the maximum $\eta_{th,\ bot}$ is 17.76% for benzene. Table 6 posts some key thermodynamic indicators by using benzene.

Table 5. Thermodynamic parameters at the optimum condition when the bottom cycle fluid is benzene.

	T (°C)	*p* (kPa)	*h* (kJ/kg)	*s* (kJ·kg^{-1}·K^{-1})
1	400	1090	1005.77	4.5671
2	353.73	105.69	932.08	4.5879
3	288.49	100.69	807.64	4.3513
4	257	100.69	457.78	3.6941
5	258.52	1160	459.32	3.7004
6	313.23	1125	583.76	3.9230
7	257	100.69	751.76	4.2489
8	214.62	6.33	683.11	4.2739
9	172.27	5.70	617.41	4.1222
10	153	5.13	243.32	3.2450
11	152.99	105.69	243.45	3.2450
12	186.39	100.69	309.14	3.3934
13	143	503.67	469.98	1.1532
14	53.41	17.61	364.65	1.2116
15	30	15.92	−91.39	−0.2784
16	30.21	538.67	−90.64	−0.2779

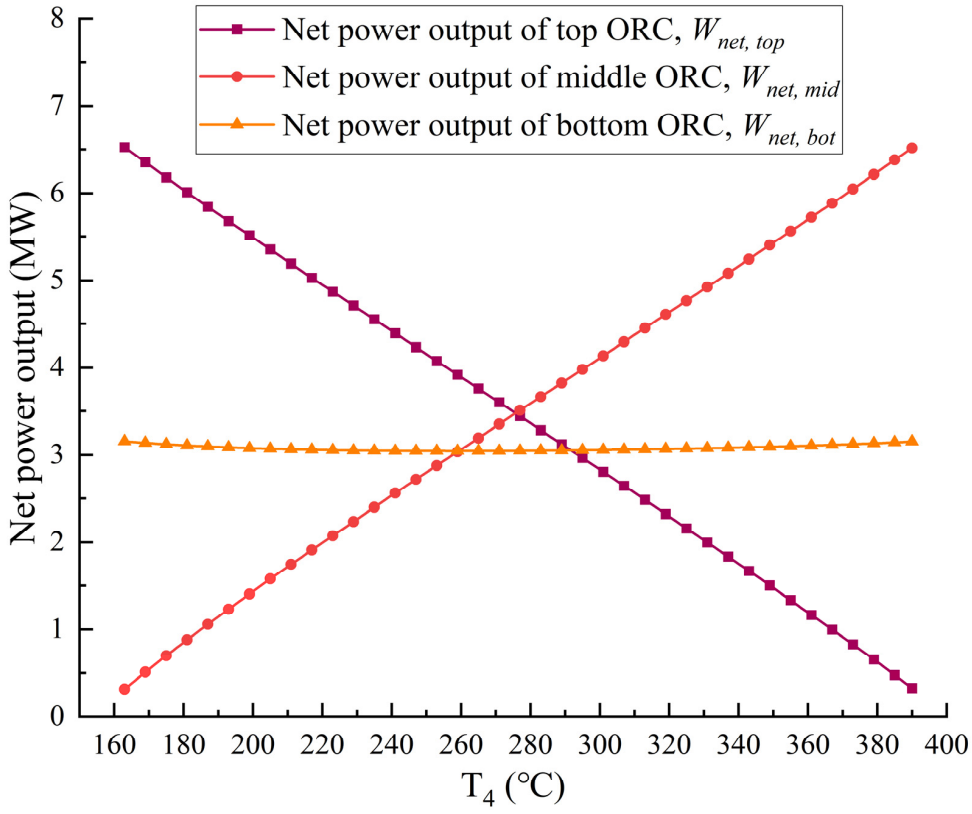

Figure 6. Variations of subcycle net power outputs for benzene when T_{10} = 153 °C.

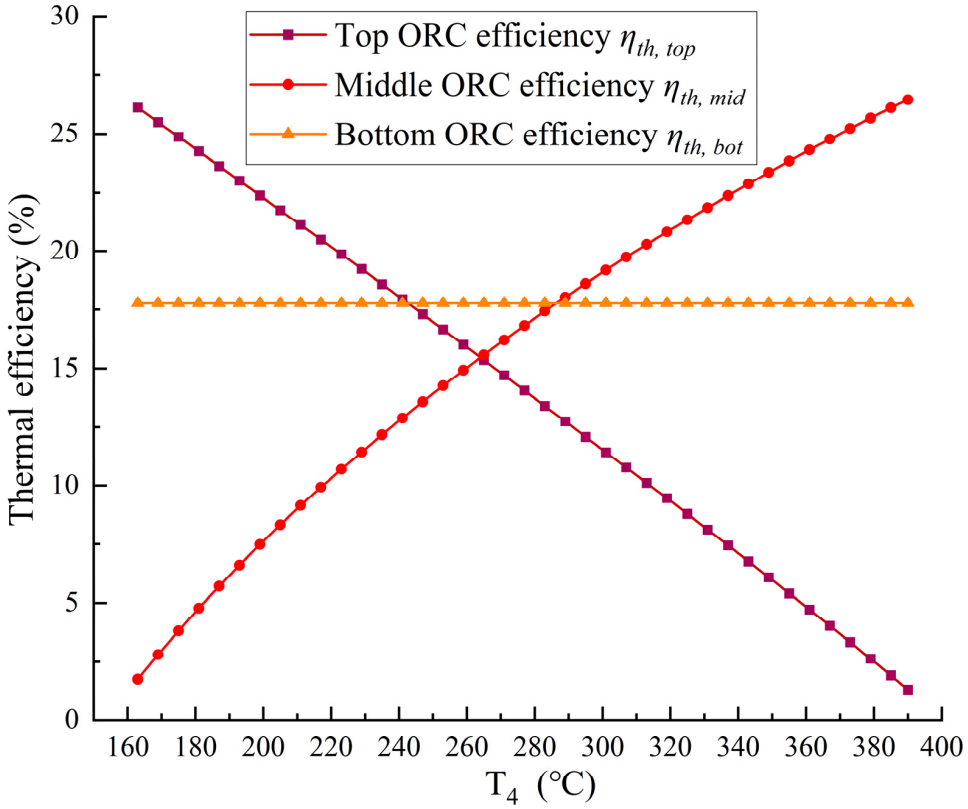

Figure 7. Variations of subcycle thermal efficiencies for benzene when $T_{10} = 153$ °C.

Table 6. Results of the parameters corresponding to the maximum.

	Top ORC	Middle ORC	Bottom ORC	TORC
m (kg/s)	57.99	45.84	30.59	-
W_T (MW)	4.27	3.15	3.23	10.65
W_P (MW)	0.089	0.006	0.023	0.118
W_{net} (MW)	3.97	2.98	3.05	10
Q (MW)	24.47	20.29	17.15	24.47
η_{th} (%)	16.22	14.71	17.76	40.86
η_{ex} (%)	28.95	33.19	67.17	72.94

4.1.2. Mass Flow Rate

Figure 8 portrays the variations of subcycle mass flow rates on the use of benzene when T_{10} is 153 °C. The mass flow rate of top ORC (m_{top}) first increases appreciably, and then soars with T_4. The reason is as follows. Given T_1 and h_1, h_6 increases with T_4 and ($h_1 - h_6$) reduces. As the net power output of TORC system ($W_{net,\ TORC}$) is fixed at 10 MW, $\eta_{th,\ TORC}$ is inversely proportional to the total heat absorbed (Q_{top}) according to Equation (25). As $\eta_{th,\ TORC}$ rises when $T_4 < 257$ °C and falls down when $T_4 > 257$ °C as displayed in Figure 5, Q_{top} first diminishes, and then increases. However, the magnitude of Q_{top} reduction is smaller than that of ($h_1 - h_6$) when T_4 ranges from 163 °C to 257 °C. For instance, Q_{top} is 24.78, 24.62 and 24.53 MW when T_4 is 180, 200 and 220 °C. The corresponding ($h_1 - h_6$) is 545.82, 512.82 and 480.44 kJ/kg. m_{top} increases moderately when 163 °C $< T_4 <$ 257 °C according to $m_{top} = \frac{Q_{top}}{h_1 - h_6}$. As Q_{top} rises and ($h_1 - h_6$) descends when $T_4 > 257$ °C, m_{top} therefore grows considerably. The mass flow rate of middle ORC (m_{mid}) decreases and the mass flow rate of bottom ORC (m_{bot}) remains almost constant with T_4. The reasons can be deduced similarly.

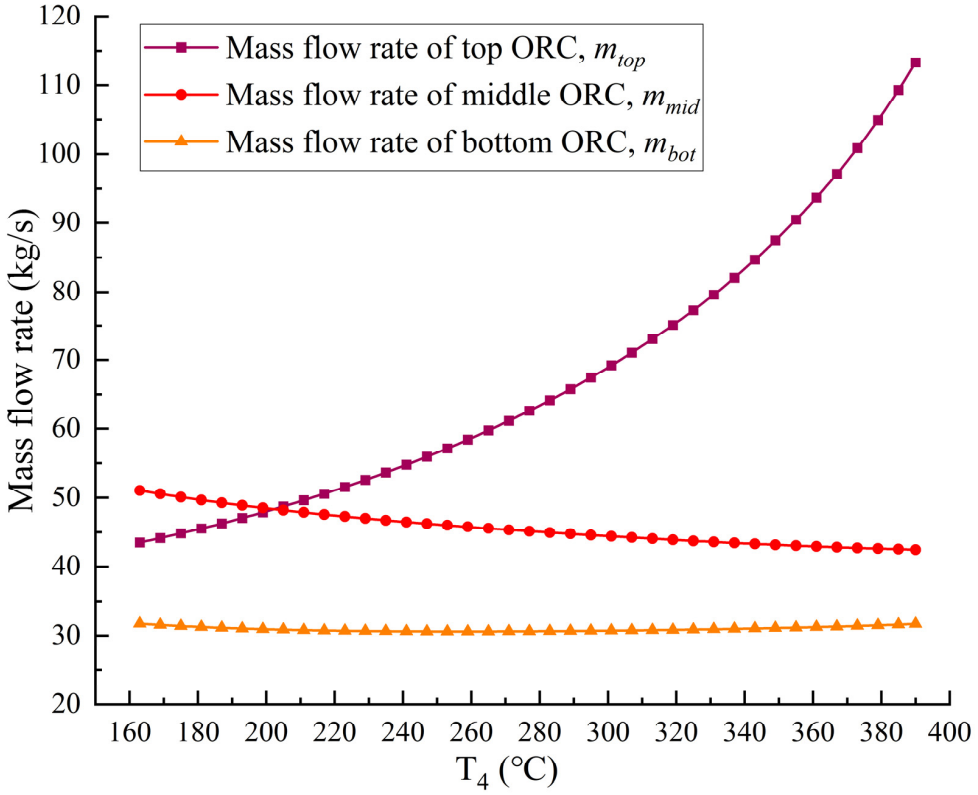

Figure 8. Variations of subcycle mass flow rates for benzene when T_{10} = 153 °C.

4.1.3. *T-Q* Diagram

Figure 9 illustrates the *T-Q* diagram at the optimum condition. The dotted lines distinguish different heat exchangers. The heat transfer temperature difference takes place at the pinch point for HX1, HX4, and HX5, while it occurs at the high temperature BDO mixture outlet for HX2 and HX3. The heat transfer temperature differences are 11.31, 29.97, 19.28, 10, and 10.26 °C for HX1–HX5, respectively. Notably, ΔT_{min} of 10 °C is the minimum heat transfer temperature difference in all the HXs. The heat transfer temperature differences in HX1, HX2, HX3, and HX5 are higher than ΔT_{min}. The heat transfer in HX1–HX5 is 24.472, 7.216, 3.012, 17.443, and 13.942 MW, respectively.

4.1.4. Entropy Generation

Figure 10 exhibits the percentage of entropy generated by each component at the maximum $\eta_{th,\ TORC}$. The largest exergy destruction takes place in HX4, which accounts for more than 30% of the total irreversible losses. This is mainly due to the large heat transfer temperature difference in the subcooled region of HX4. The cold side benzene rises from a subcooled state at 30.21 °C to a saturated liquid state at 143 °C, while the hot side BDO mixture remains in the binary phase state of 153 °C. The entropy generation in T3 ranks the second largest on account of the large enthalpy drop (i.e., exergy drop) during expansion. The irreversible loss in P3 accounts for merely 0.1%, which is much less than that of P1 and P2. The reason is that the mass flow rate through P3 (m_{bot} = 30.59 kg/s) is remarkably lower than that of P1 (m_{top} = 57.99 kg/s) and P2 (m_{mid} = 45.84 kg/s).

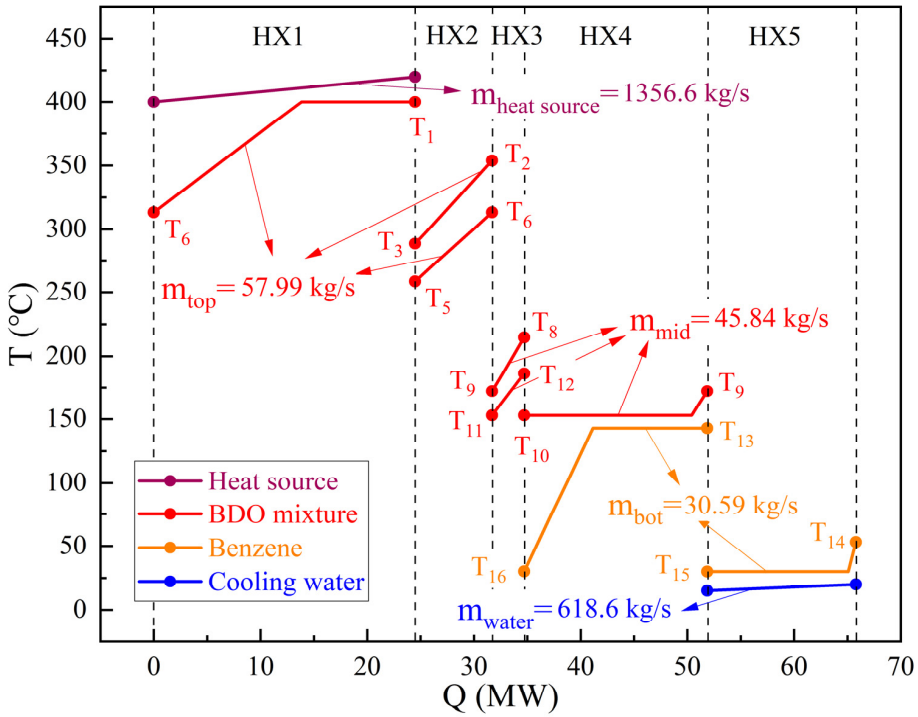

Figure 9. *T-Q* diagram at the optimal condition.

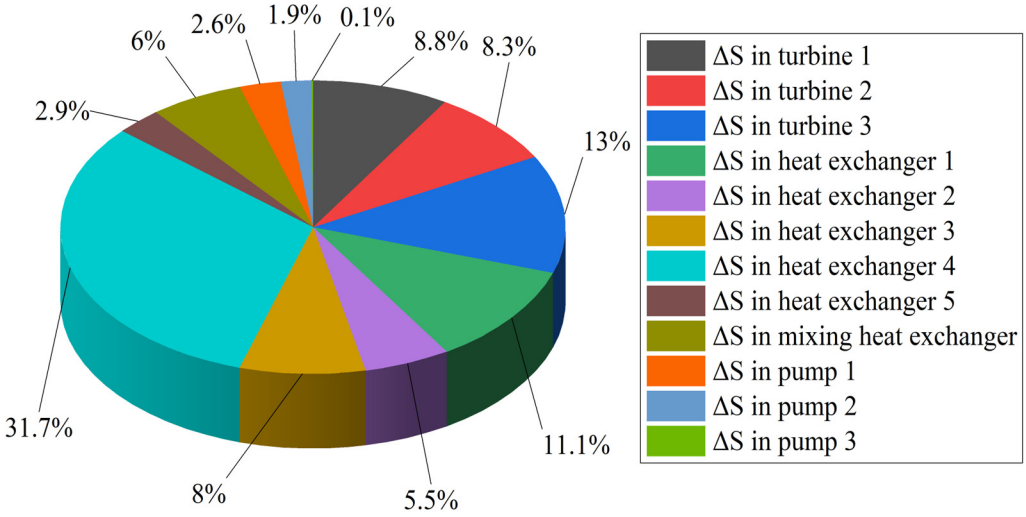

Figure 10. Entropy generation in the TORC on the use of benzene.

4.1.5. Exergy Efficiency

Figure 11 graphs the variation of $\eta_{ex,\ TORC}$ with T_4 and T_{10}. Similar to Figure 4, the area of the curved surface representing pentane and R141b is smaller than that of benzene and cyclohexane due to the narrower T_{10} range. Benzene has very close exergy efficiencies, and pentane has the lowest $\eta_{ex,\ TORC}$. Given T_4, $\eta_{ex,\ TORC}$ drops monotonously as T_{10} elevates. The optimal $\eta_{ex,\ TORC}$ is obtained at the lowest T_{10} of 153 °C for different bottom ORC fluids, which is the same as that of $\eta_{th,\ TORC}$.

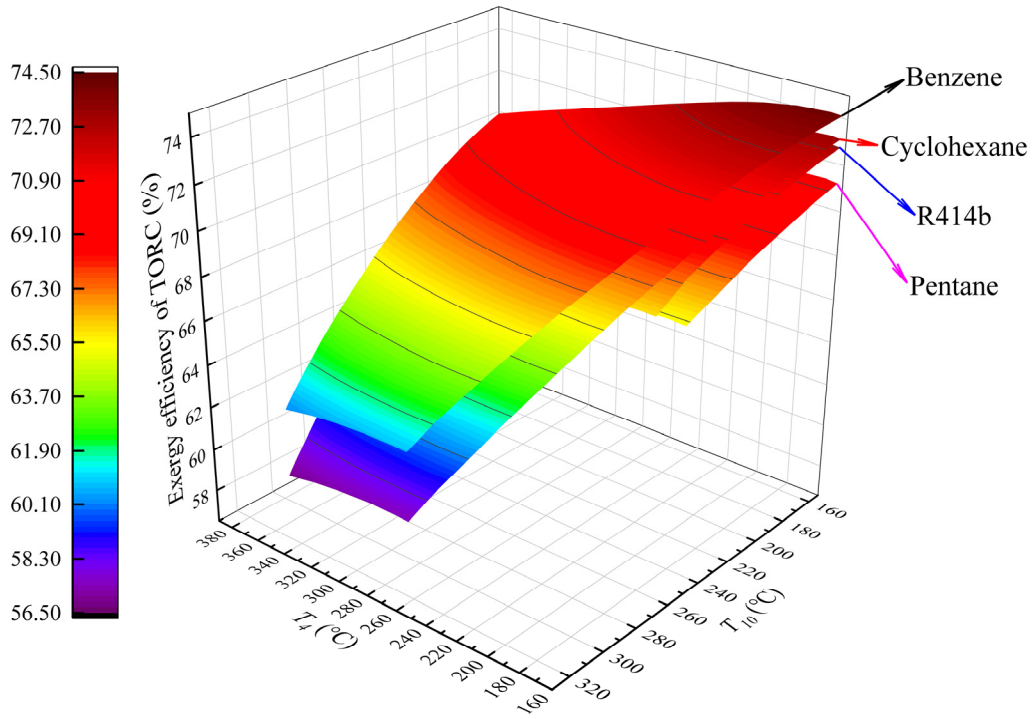

Figure 11. Variations of TORC exergy efficiency with T_4 and T_{10}.

Given the top ORC evaporation and bottom ORC condensation temperatures, both the system thermal and exergy efficiencies decrease with the increment in T_{10}. It indicates that a smaller temperature difference in the bottom ORC is more beneficial to the overall thermodynamic performance.

Figure 12 shows the cross section of the above three-dimensional diagram corresponding to T_{10} of 153 °C. All the curves first climb marginally, and then go down considerably. The peak value of each curve is achieved when T_4 is 172 °C. The maximum $\eta_{ex,TORC}$ is 74.14% for benzene, which indicates that the TORC system has the highest degree of thermodynamic perfection when benzene is adopted. It is worth pointing out that the maximum thermal and exergy efficiencies correspond to the same middle ORC condensation temperatures of 153 °C, but to different MHX outlet temperatures.

4.2. Economic Assessment

Benzene is exemplified in this section due to its highest $\eta_{th,\ TORC}$ and $\eta_{ex,\ TORC}$. The economic calculation is based on the parameters in Table 5.

4.2.1. Design of HXs

Heat Transfer Research Inc. (HTRI, located in Navasota, TX, USA) technology has been used by companies worldwide for decades to design, operate, and maintain HXs and fired heaters. The acclaimed Xchanger Suite® software (Version 7.3.2) is applied in this section as it is considered the most advanced available for the design, rating, and simulation of HXs [49].

The most widely used shell-and-tube HXs are exemplified. The hot and cold fluids are located in the shell and tube sides, respectively. Double tube passes with the tube outer diameter of 19 mm and the tube pitch of 25 mm are employed, which are frequent in industrial production. The ratio of the tube length and the shell inner diameter is limited to 4–10, and the over-design area above 10% is ensured in the design process. The introduction of rod baffles can remarkably increase the flow rate while reducing the vibration and the flow resistance of the shell side fluid. The shell side fluid makes an axial flow parallel to the tube bundle, which facilitates uniform vortices along the tube length and on the heat

transfer surfaces. The vortices are good for improving the parallel flow heat transfer. In consequence, rod baffles are exploited in HX1–HX5.

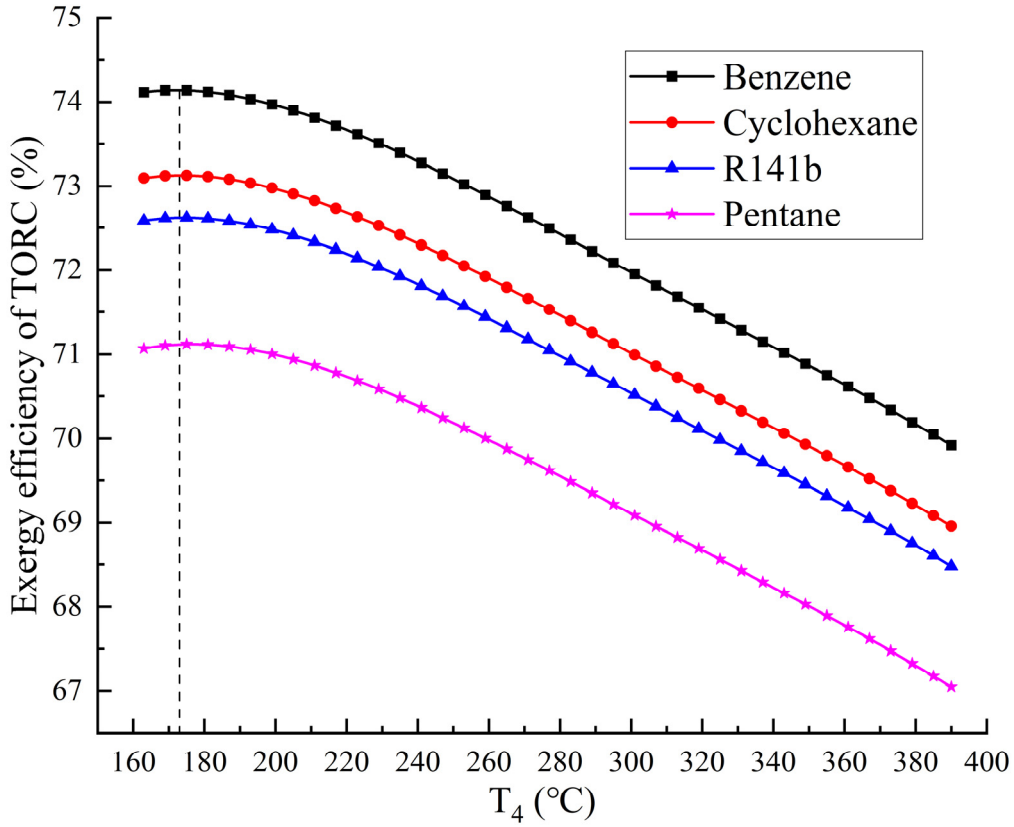

Figure 12. Variations of TORC exergy efficiency with T_4 when $T_{10} = 153$ °C.

The key physical data of the BDO mixture can be referred directly to Aspen Plus [50] by inputting a mass fraction of 73.5% diphenyl oxide and 26.5% biphenyl. Then the parameters such as heat capacity, density, dynamic viscosity, and thermal conductivity can be imported from Aspen Plus into Xchanger Suite. As the fouling resistances of organic heat carriers for industrial use, solvent vapor, refrigerant liquid, and cooling water below 52 °C are all 17.6×10^{-5} m^2·K/W according to GB/T 151-2014 [51], the fouling resistances of BDO mixture, benzene, and water in this work are taken as 17.6×10^{-5} m^2·K/W. 420 °C industrial flue gas is exemplified as heat source, and its fouling resistance is 176.1×10^{-5} m^2·K/W [52]. The dominating composition of flue gas is air, and its physical parameters can be invoked from REFPROP 8.0 [53]. Table 7 provides the design data of different HXs and Figure 13 portrays the schemes.

Table 7. Design parameters of different HXs.

	HX1	HX2	HX3	HX4	HX5
Type	BJM	BES	BEM	BEM	BJM
Shell side heat transfer coefficient, W/m^2·K	68,345	311.75	223.80	247.43	1486.3
Tube side heat transfer coefficient, W/m^2·K	1135.3	684.35	210.49	609.96	11,485
Shell ID, mm	2100	1700	1900	1900	1400
Tube length, m	16	144	9	10	10
Ratio of tube length and shell ID	7.62	88.24	4.74	5.26	7.14
Tube count	3359	2774	4972	4612	2506
Overall heat transfer coefficient, W/m^2·K	611.36	181.64	91.51	152.48	819.90

Table 7. *Cont.*

	HX1	HX2	HX3	HX4	HX5
Heat duty, MW	27.230	7.9854	3.3410	9.2282	14.362
Baffle central spacing, mm	800	1000	800	800	1000
Effective mean temperature difference, °C	16	21.9	16.2	24.7	13.3
Area, m^2	3118.9	2291.8	2631.4	2716.2	1475.4
Over design, %	12.27	14.13	16.60	10.71	11.78

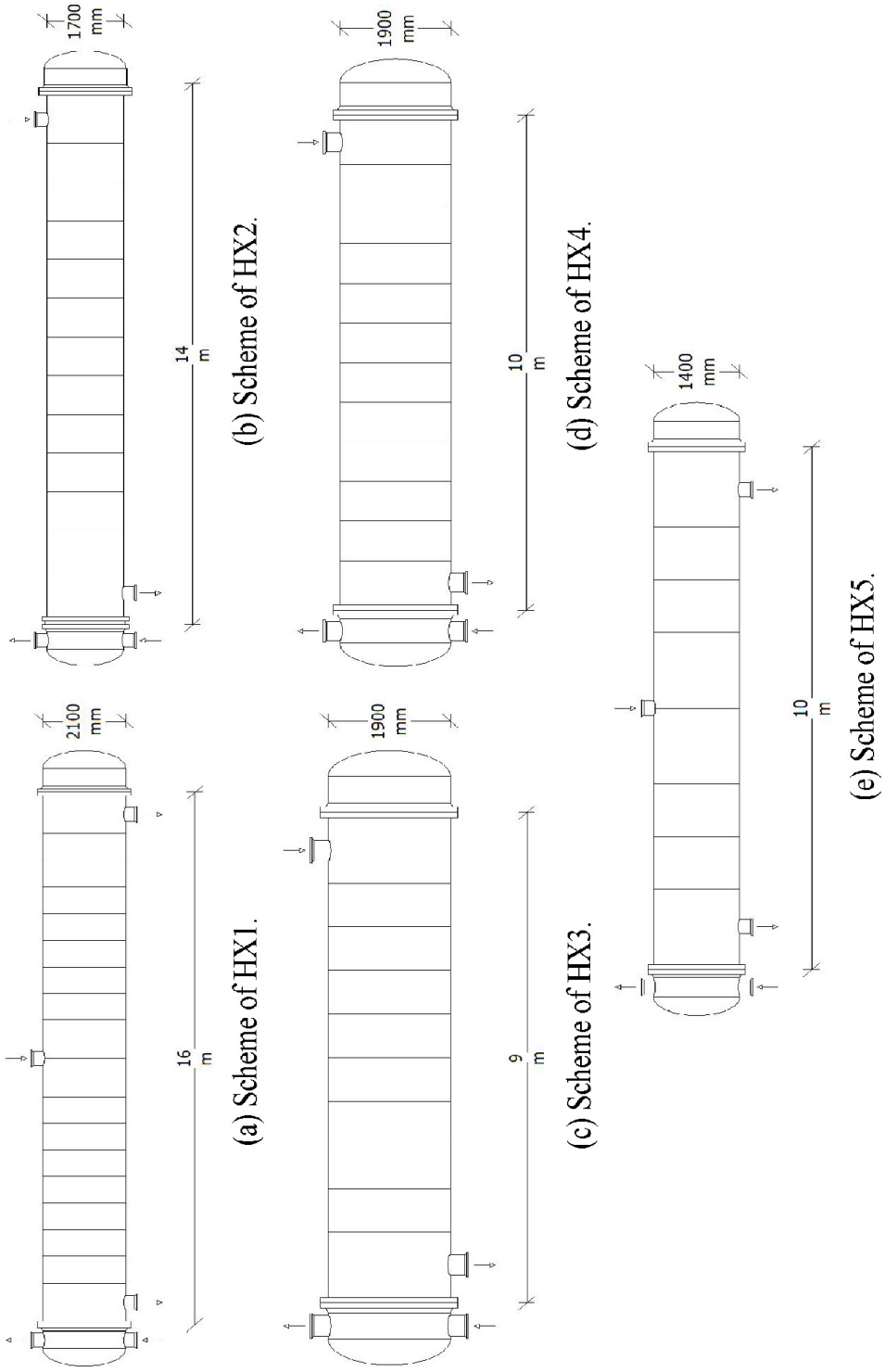

Figure 13. Schemes of the shell and tube HXs.

4.2.2. Material Selection and Initial Investment

The choice of construction materials is a compromise between the conflicting goals of performance and capital cost. Multiple factors need to be considered, including mechanical properties (mainly strength), oxidation resistance, heat resistance, and corrosion resistance, etc. [53]. The operating temperatures of *HX*1 and *T*1 reach 400 °C, which imposes stringent requirements for materials. Although stainless steel is somewhat more expensive than carbon steel, its various properties and lifespan in the range of 400 to 500 °C are superior to those of carbon steel [53–55]. In view of this, *HX*1 and *T*1 are manufactured in stainless steel and carbon steel for the remaining equipment. Table 8 indexes the selected impact factors of the devices [29,53].

Table 8. Values of constants for HXs and turbines.

	F_M	F_P	F_T
HX1	2.9	1	1
HX2	1	1	1
HX3	1	1	1
HX4	1	1.3	1
HX5	1	1.3	1
T1	3.2	1	1
T2	1	1.3	1
T3	1	1	1

The power generated by *T*1 ($W_{top} \cdot \varepsilon_G$), *T*2 ($W_{mid} \cdot \varepsilon_G$) and *T*3 ($W_{bot} \cdot \varepsilon_G$) is 4.059 MW, 2.990 MW and 3.069 MW, respectively. M_{BDO} and the mass of benzene ($M_{benzene}$) are 38,064.6–39,262.9 kg and 16,572.6–17,094.3 kg according to Section 3.2.2. For the sake of sufficient charge mass and reliable results, M_{BDO} and $M_{benzene}$ are taken as 40,000 kg and 18,000 kg, respectively. As P_{BDO} is 2.2 USD/kg [56] and $P_{benzene}$ is 0.92 USD/kg [57], the total cost of the two fluids is 10.46 $\times$ 10^4 USD.

Table 9 summarizes the first cost of each component. The total cost of the TORC system is 2704.40 $\times$ 10^4 USD. The cost of T1 accounts for the largest proportion, followed by T3 and T2. The three turbines occupy more than three quarters and the five HXs account for nearly one fifth of the total investment. It can be calculated that LEC is 0.0368 USD/kWh. It is worth pointing out that $\eta_{th,\ TORC}$ in this work is more efficient than that claimed by all the predecessors. Meanwhile, LEC is lower than the indicators obtained by existing TORCs. Table 10 presents a comparison between the results of this study and those of others.

Table 9. Investment cost of each component.

Component	Cost ($\times 10^4$ USD)	Component	Cost ($\times 10^4$ USD)	Component	Cost ($\times 10^4$ USD)
HX1	233.99	HX2	65.43	HX3	71.88
HX4	95.48	HX5	63.05	T1	1361.28
T2	343.39	T3	349.73	P1	16.29
P2	3.93	P3	7.12	G1	32.76
G2	24.50	G3	25.11		

Table 10. Comparison with the previous studies.

	Heat Source/Cold Source	Maximum Evaporation Temperature (°C)	Top/Middle/Bottom Fluid	η_{th} (%)	η_{ex} (%)	LEC (USD/kWh)
Prabhu et al. [2]	Therminol/air	318	Toluene/cyclohexane/butane	27.5	-	-
Mahmoud et al. [3]	Waste heat/cooling water	160	Hydrocarbon	-	-	-
Zhang et al. [4]	Air/cooling water	300	R245fa/r152a/CO	26.86	79.46	0.063
Yu et al. [5]	Geothermal water/ cooling water	200	R245fa	-	-	0.04
García et al. [6]	Residual heat/LNG	60	Argon/methane/R14	-	85.6	-

Table 10. *Cont.*

	Heat Source/Cold Source	Maximum Evaporation Temperature (°C)	Top/Middle/Bottom Fluid	η_{th} (%)	η_{ex} (%)	LEC (USD/kWh)
Zhang et al. [7]	Low-temperature waste heat/LNG	46.85	R245fa	32.5	39.08	-
Han et al. [8]	Waste heat/LNG	127.17	R290/R601a/R236ea	-	-	-
TORC in this paper	Waste heat/cooling water	400	BDO/BDO/benzene	40.86	74.14	0.0368

5. Comparison with a Cascade ORC Using the BDO Mixture

A BDO cycle bottomed by a benzene cycle is depicted in Figure 14 as a reference to determine whether the proposed TORC can boost efficiency and drive down cost compared with the cascade ORC. The conditions of cold and heat sources are identical to those in Figure 2, as well as the equipment efficiencies. T4 inlet temperature (T_{17}) and bottom cycle condensation temperature (T_{25}) are respectively 400 °C and 30 °C. Figure 15 presents the variations of the cascade efficiencies. The maximum thermal and exergy efficiencies are respectively 39.84% and 74.14% at the lowest T_{20} of 153 °C. Table 11 reports the thermodynamic parameters for cascade ORC at the optimum condition.

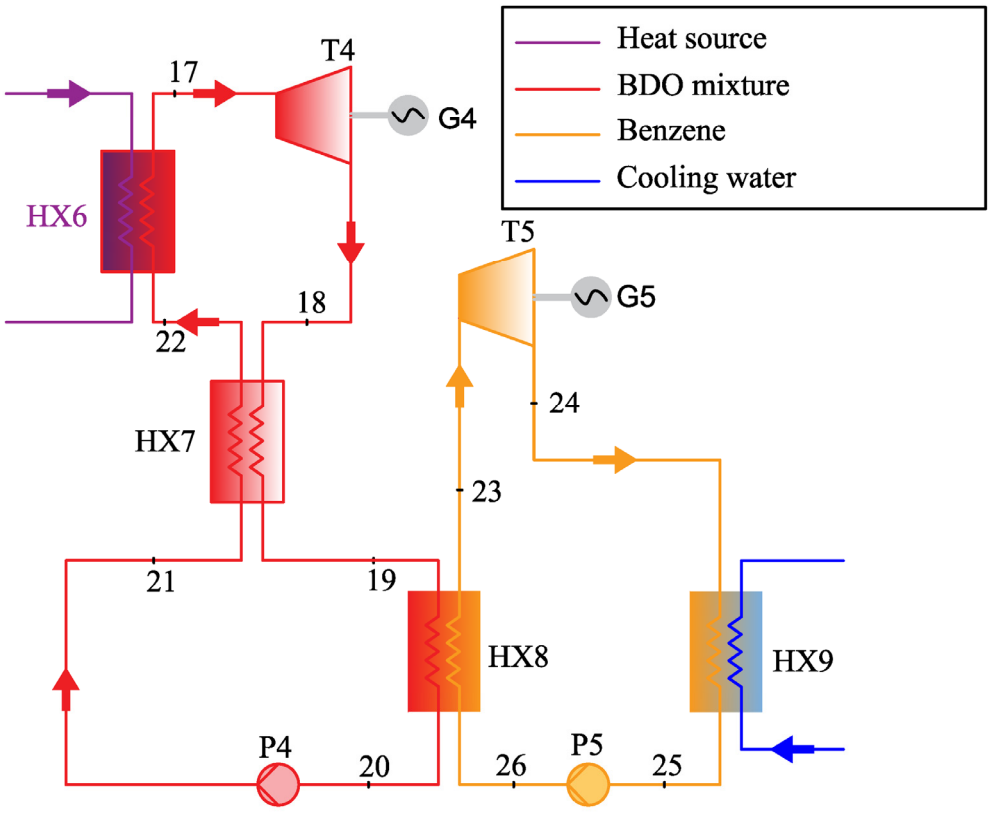

Figure 14. Schematic diagram of the cascade ORC.

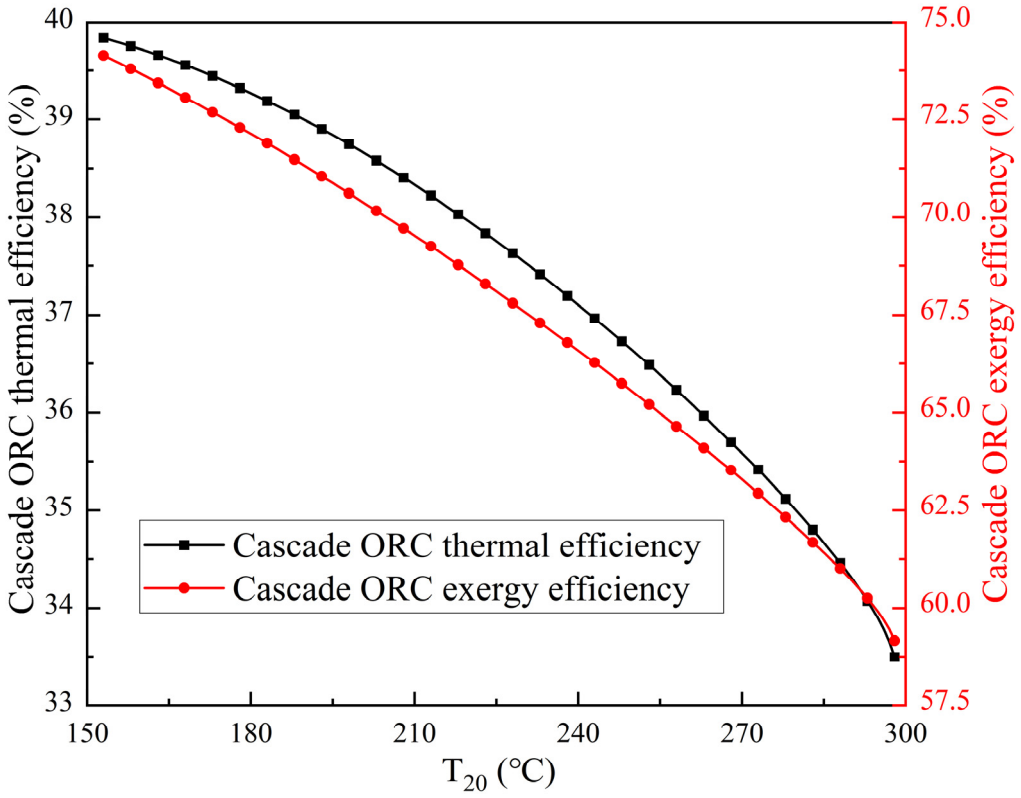

Figure 15. Variations of the cascade ORC thermal and exergy efficiencies with T_{20}.

Table 11. Thermodynamic parameters of the cascade ORC at the optimum condition.

	T (°C)	*p* (kPa)	*h* (kJ/kg)	*s* (kJ·kg^{-1}·K^{-1})
17	400	1090	1005.77	4.5671
18	302.54	6.33	835.25	4.6201
19	203.75	5.7	665.75	4.2270
20	153	5.13	243.32	3.245
21	155.68	1160	244.83	3.2571
22	238.96	1125	414.33	3.6174
23	143	503.67	469.98	1.1532
24	53.03	17.61	364.23	1.2119
25	30	15.92	−91.39	−0.2784
26	30.21	538.67	−90.79	−0.2779

Tables 12 and 13 list the HX design parameters and initial cost. HX6 and T4 are made of stainless steel due to the 400 °C operation temperature, and the others are carbon steel. The power generated by T4 and T5 is 7.056 MW and 3.297 MW, respectively. M_{BDO} is 36,196.2–37,335.7 kg and $M_{benzene}$ is 16,572.6–16,918.2 kg theoretically. In the same vein, M_{BDO} and $M_{benzene}$ are taken as 38,000 kg and 18,000 kg, respectively. The total cost of the two fluids is 10.02 × 10^4 USD and the overall cost of the cascade ORC system is 2866.81 × 10^4 USD. It can be calculated that LEC is 0.04 USD/kWh, which is higher than that of the TORC system.

Table 12. Design parameters of the HXs in cascade ORC.

	HX6	HX7	HX8	HX9
Type	BJM	BES	BES	BEM
Shell side heat transfer coefficient, $W/m^2 \cdot K$	70,939	190.63	953.18	1439.4
Tube side heat transfer coefficient, $W/m^2 \cdot K$	976.58	434.62	564.03	9541.7
Shell ID, mm	2000	1800	2100	1500
Tube length, m	14	13	16	8
Ratio of tube length and shell ID	7	7.22	7.62	5.33
Tube count	2978	2774	5246	2535
Overall heat transfer coefficient, $W/m^2 \cdot K$	576.69	116.22	267.68	791.08
Heat duty, MW	26.878	7.7654	17.345	13.718
Baffle central spacing, mm	800	1000	800	1000
Effective mean temperature difference, °C	22.0	35	13.5	14.1
Area, m^2	2427.1	2126.3	5581.4	1382.0
Over design, %	14.54	11.41	16.27	12.28

Table 13. Investment cost of each component in cascade ORC.

Component	Cost ($\times 10^4$ USD)	Component	Cost ($\times 10^4$ USD)	Component	Cost ($\times 10^4$ USD)
HX6	197.30	HX7	62.18	HX8	150.07
HX9	60.31	T4	1933.77	T5	354.79
P4	12.83	P5	7.19	G4	52.75
G5	25.61				

6. Conclusions

This paper proposes a novel high-temperature TORC system using the near-azeotropic mixture BDO as the top and middle ORC working fluid, and common organic fluids for the bottom ORC. The following conclusions can be drawn:

(1) The optimum thermodynamic property is achieved when benzene is adopted as the bottom ORC fluid. The maximum thermal and exergy efficiencies are respectively 40.86% and 74.14%. HX4 accounts for the largest entropy generation (>30%), followed by T3 and HX1.

(2) Given the total net power output of 10 MW, the investment cost of the TORC system is 2704.40 $\times$ 10^4 USD. The three turbines account for more than 75% and the five HXs occupy nearly 20% of the total investment. The levelized energy cost (LEC) is 0.0368 USD/kWh, which is appreciably lower than that of the existing TORC systems.

(3) The TORC outperforms the BDO mixture-based cascade ORC by 1.02% in thermal efficiency, while saving the LEC by 0.0032 USD/kWh. It demonstrates that the TORC is more favorable under the condition of 400 °C heat source.

7. Future Work

A plan to build a small-scale TORC system has been made, starting from tests of the thermodynamic cycle using the BDO mixture. Due to the high evaporation temperature, the proposed TORC is especially suitable for heat-to-power conversion in concentrated solar power systems and Carnot batteries, where phase change materials (PCMs) can be used for thermal storage. Thermo-economic investigation on the TORC coupled with PCMs will be useful. Besides, coupling the BDO mixture-based ORC with other high-temperature power cycles such as the supercritical carbon dioxide cycle or gas-turbine cycle is worth exploring. Finally, alkaline metals with higher critical temperatures (such as cesium, rubidium, potassium, and sodium) can be considered in TORC or multi-stage ORC configurations to increase the cycle efficiency further.

Author Contributions: Conceptualization, J.L.; methodology, Y.W.; software, X.R., Y.W. and X.L.; validation, Y.C. and X.R.; formal analysis, C.S.; investigation, P.L. and D.J.; resources, X.L.; data curation, J.L. and Y.C.; writing—original draft preparation, P.L.; writing—review and editing, C.S.; supervision, D.J. All authors have read and agreed to the published version of the manuscript.

Funding: This study was sponsored by National Natural Science Foundation of China (52206008), Fundamental Research Funds for the Central Universities of China (JZ2022HGTB0266), Science and Technology Major Project of Anhui Province (202003a05020025), Dongfang Electric Dongfang Boiler Group Co., Ltd.

Data Availability Statement: No new data were created or analyzed in this study. Data sharing is not applicable to this article.

Conflicts of Interest: The authors declare that this study received funding from Dongfang Boiler Co., Ltd. The funder had the following involvement with the study: investigation and writing—original draft preparation. The remaining authors declare that the research was conducted in the absence of any commercial or financial relationships that could be construed as a potential conflict of interest.

References

1. Dumont, O.; Frate, G.F.; Pillai, A.; Lecompte, S.; De Paepe, M.; Lemort, V. Carnot battery technology: A state-of-the-art review. *J. Energy Storage* **2020**, *32*, 101756. [CrossRef]
2. Prabhu, E. *Solar Trough Organic Rankine Electricity System (STORES) Stage 1: Power Plant Optimization and Economics. November 2000–May 2005*; N. p; U.S. Department of Commerce National Technical Information Service: Springfield, VA, USA, 2006. [CrossRef]
3. Mahmoud, M.; Mohammed, H.; Saleh, A. Oil and Gas Refining and Marketing Companies; Patent Issued for Power Generation Using Independent Triple Organic Rankine Cycles from Waste Heat in Integrated Crude Oil Refining and Aromatics Facilities. SA, 19178021.2. Available online: https://patentimages.storage.googleapis.com/0f/8f/f1/04c69a73bd2aee/EP3553287B1.pdf (accessed on 23 November 2023).
4. Zhang, Y.F.; Gong, L.; Hung, T.C. Innovative arrangements of multiple organic Rankine cycles to effectively generate power from the medium-to-low grade of heat source. *Appl. Therm. Eng.* **2021**, *193*, 116960. [CrossRef]
5. Yu, H.; Lu, X.L.; Zhang, W.; Zhang, J. Thermodynamic and Techno-economic Analysis of a Triple-pressure Organic Rankine Cycle: Comparison with Dual-pressure and Single-pressure ORCs. *Acta Geol. Sin.* **2021**, *95*, 1857–1869. [CrossRef]
6. García, R.F.; Carril, J.C.; Gomez, J.; Gomezet, M.R. Power Plant Based on Three Series Rankine Cycles Combined with a Direct Expander Using LNG Cold as Heat Sink. *Energy Convers. Manag.* **2015**, *101*, 285–294. [CrossRef]
7. Zhang, M.G.; Zhao, L.J.; Xiong, Z. Optimization and analyses of organic Rankine cycle combined system utilizing cold energy of LNG and industrial waste heat. *CIESC J.* **2014**, *65*, 3144–3151. [CrossRef]
8. Han, F.H.; Wang, Z.; Ji, Y.L.; Lia, W.H.; Sundénc, B. Energy Analysis and Multi-Objective Optimization of Waste Heat and Cold Energy Recovery Process in LNG-Fueled Vessels Based on a Triple Organic Rankine Cycle. *Energy Convers. Manag.* **2019**, *195*, 561–572. [CrossRef]
9. Dai, X.Y.; An, Q.S.; Shi, L. Experiment research for the thermal stability of isobutene and isopentane. *J. Eng. Therm.* **2013**, *34*, 1416–1419. Available online: https://www.researchgate.net/publication/289013198_Experiment_research_for_the_thermal_stability_of_isobutene_and_isopentane (accessed on 23 November 2023).
10. Therminol® VP-1 by Application. Available online: https://www.therminol.com/applications/organic-rankine-cycle#_ga (accessed on 5 August 2023).
11. Therminol® VP-1 Heat Transfer Fluid. Available online: https://www.therminol.com/product/71093459?pn=Therminol-VP-1-Heat-Transfer-Fluid (accessed on 5 August 2023).
12. Vishwakarma, S.; Debnath, B.K.; Debnath, K. Comparative analysis of absorber tubes of parabolic trough solar collector using Therminol VP-1 as heat transfer fluid. In *Advances in Mechanical Engineering*; Springer: Singapore, 2020; pp. 1227–1240. [CrossRef]
13. Bronicki, L.Y. The Ormat Rankine Power Unit. In Proceedings of the 7th Intersociety Energy Conversion Engineering Conference, San Diego, CA, USA, 25 September 1972; pp. 327–334.
14. Bombarda, P.; Invernizzi, C. Binary Liquid Metal-Organic Rankine Cycle for Small Power Distributed High Efficiency Systems. *Proc. Inst. Mech. Eng. Part A J. Power Energy* **2014**, *229*, 192–209. [CrossRef]
15. Vescovo, R.; Spagnoli, E. High temperature orc systems. *Energy Procedia* **2017**, *129*, 82–89. [CrossRef]
16. Vescovo, R. High temperature organic rankine cycle (ht-orc) for cogeneration of steam and power. *AIP Conf. Proc.* **2019**, *2191*, 020153. [CrossRef]
17. Sampedro, E.O.; Védie, L. Wet to dry cycles for high temperature waste heat valorisation using a diphenyl-biphenyl oxide mixture. In Proceedings of the 6th International Seminar on ORC Power Systems, Munich, Germany, 11–13 October 2021; pp. 1–10. [CrossRef]
18. Li, P.C.; Li, J. High-temperature Direct Vapor Generation Organic Rankine Cycle in the Concentrated Solar Power Application. In Proceedings of the 6th International Seminar on ORC Power Systems, Munich, Germany, 11–13 October 2021.

19. Li, P.C.; Ye, J.; Li, J.; Wang, Y.D.; Jiang, X.B.; Qian, T.L. Thermodynamic and techno-economic analysis of a direct thermal oil vaporization solar power system. *Energy* **2023**, *282*, 128963. [CrossRef]
20. Ren, X.; Li, J.; Pei, G.; Li, P.C.; Gong, L. Parametric and Economic Analysis of High-temperature Cascade Organic Rankine Cycle with a Biphenyl and Diphenyl Oxide Mixture. *Energy Convers. Manag.* **2023**, *276*, 116556. [CrossRef]
21. Li, P.C.; Qian, T.L.; Li, J.; Lin, H.W.; Wang, Y.D.; Pei, G. Thermo-economic analysis of a novel partial cascade organic-steam Rankine cycle. *Energy Convers. Manag.* **2023**, *283*, 116941. [CrossRef]
22. Dincer, I. 1.6 Energy. In *Comprehensive Energy Systems*; Elsevier: Amsterdam, The Netherlands, 2018; pp. 212–264. [CrossRef]
23. Gao, G.T.; Li, J.; Li, P.C.; Yang, H.L.; Pei, G.; Ji, J. Design and analysis of an innovative concentrated solar power system using cascade organic Rankine cycle and two-tank water/steam storage. *Energy Convers. Manag.* **2021**, *237*, 114108. [CrossRef]
24. Önsan, Z.I.; Avci, A.K. Chapter 14—Reactor Design for Fuel Processing. In *Fuel Cells: Technologies for Fuel Processing*; Elsevier: Amsterdam, The Netherlands, 2011; pp. 451–516. [CrossRef]
25. Mukherjee, R. *Practical Thermal Design of Shell-and-Tube Heat Exchangers*; Begell House Inc.: Danbury, CT, USA, 2004.
26. EASTMAN. Therminol ®VP-1 Heat Transfer Fluid [EB/OL]. Available online: https://www.eastman.com/Literature_Center/T/TF9141.pdf (accessed on 5 August 2023).
27. Xu, P.C.; Zou, Z.P.; Yao, L.C. A unified performance conversion method for similar compressors working with different gases based on polytropic analysis and deep-learning improvement. *Energy Convers. Manag.* **2021**, *247*, 114747. [CrossRef]
28. Li, J.; Alvi, J.Z.; Pei, G.; Su, Y.H.; Li, P.C.; Gao, G.T. Modelling of organic Rankine cycle efficiency with respect to the equivalent hot side temperature. *Energy* **2016**, *115*, 668–683. [CrossRef]
29. Turton, R.; Bailie, R.C.; Whiting, W.B.; Shaeiwit, J.A. *Analysis, Synthesis, and Design of Chemical Processes*, 4th ed.; Prentice Hall PTR: New Jersey, NJ, USA, 2013.
30. Kose, O.; Koc, Y.; Yagli, H. Energy, exergy, economy and environmental (4E) analysis and optimization of single, dual and triple configurations of the power systems: Rankine Cycle/Kalina Cycle, driven by a gas turbine. *Energy Convers. Manag.* **2021**, *227*, 113604. [CrossRef]
31. Eduardo, J.C.C.; Motta, H.P. Exergoeconomic analysis of a solar-powered/fuel assisted Rankine cycle for power generation. *Energy* **2015**, *88*, 555–562. [CrossRef]
32. Li, P.C.; Cao, Q.; Li, J.; Lin, H.W.; Wang, Y.D.; Gao, G.T. An innovative approach to recovery of fluctuating industrial exhaust heat sources using cascade Rankine cycle and two-stage accumulators. *Energy* **2021**, *228*, 120587. [CrossRef]
33. Cataldo, F.; Mastrullo, R.; Mauro, A.W.; Vanoli, G.P. Fluid selection of organic Rankine cycle for low-temperature waste heat recovery based on thermal optimization. *Energy* **2014**, *72*, 159–167. [CrossRef]
34. Zhang, C.; Liu, C.; Wang, S.K.; Xu, X.X.; Li, Q.B. Thermo-economic comparison of subcritical organic Rankine cycle based on different heat exchanger configurations. *Energy* **2017**, *123*, 728–741. [CrossRef]
35. Zhang, S.J.; Wang, H.X.; Guo, T. Performance comparison and parametric optimization of subcritical Organic Rankine Cycle (ORC) and transcritical power cycle system for low-temperature geothermal power generation. *Appl. Energy* **2011**, *88*, 2740–2754. [CrossRef]
36. Bai, L. *Life Cycle Assessment of Electricity Generation from Low Temperature Waste Heat: The Influence of Working Fluid*; NTNU-Norwegian University of Science & Technology: Trondheim, Norway, 2012.
37. Ding, Y.; Liu, C.; Zhang, C.; Xu, X.X.; Li, Q.B.; Mao, L.F. Exergoenvironmental model of Organic Rankine Cycle system including the manufacture and leakage of working fluid. *Energy* **2018**, *145*, 52–64. [CrossRef]
38. Sohrabi, A.; Behbahaninia, A.; Sayadi, S. Thermodynamic optimization and comparative economic analysis of four organic Rankine cycle configurations with a zeotropic mixture. *Energy Convers. Manag.* **2021**, *250*, 114872. [CrossRef]
39. Astolfi, M. Techno-economic Optimization of Low Temperature CSP Systems Based on ORC with Screw Expanders. *Energy Procedia* **2015**, *69*, 1100–1112. [CrossRef]
40. Li, Y.R.; Du, M.T.; Wu, C.M.; Wu, S.Y.; Liu, C.; Xu, J.L. Economical evaluation and optimization of subcritical organic Rankine cycle based on temperature matching analysis. *Energy* **2014**, *68*, 238–247. [CrossRef]
41. Gao, G.T.; Li, J.; Li, P.C.; Cao, J.Y.; Pei, G.; Dabwan, Y.N. Design of steam condensation temperature for an innovative solar thermal power generation system using cascade Rankine cycle and two-stage accumulators. *Energy Convers. Manag.* **2019**, *184*, 389–401. [CrossRef]
42. Wang, X.; Tian, H.; Shu, G. Part-Load Performance Prediction and Operation Strategy Design of Organic Rankine Cycles with a Medium Cycle Used for Recovering Waste Heat from Gaseous Fuel Engines. *Energies* **2016**, *9*, 527. [CrossRef]
43. Eduardo, L.M.; Ángel, M.G.; Helen, L.; Raúl, L.; Teresa, L.; Mauricio, S. Comparative Thermodynamic Analysis of the Performance of an Organic Rankine Cycle Using Different Working Fluids. *Energies* **2022**, *15*, 2588.
44. Wang, K.; He, Y.L. Thermodynamic analysis and optimization of a molten salt solar power tower integrated with a recompression supercritical CO_2 Brayton cycle based on integrated modeling. *Energy Convers. Manag.* **2017**, *135*, 336–350. [CrossRef]
45. Tabriz, Z.H.; Mohammadpourfard, M.; Akkurt, G.G.; Heris, S.Z. Energy, exergy, exergoeconomic, and exergoenvironmental (4E) analysis of a new bio-waste driven multigeneration system for power, heating, hydrogen, and freshwater production: Modeling and a case study in Izmir. *Energy Convers. Manag.* **2023**, *288*, 117130. [CrossRef]
46. El-Emam, R.S.; Dincer, I. Exergy and exergoeconomic analyses and optimization of geothermal organic Rankine cycle. *Appl. Therm. Eng.* **2013**, *59*, 1–2. [CrossRef]

47. Fernandez, F.J.; Prieto, M.M.; Suarez-Ramon, I. Thermodynamic analysis of high-temperature regenerative organic Rankine cycles using siloxanes as working fluids. *Energy* **2011**, *36*, 5239–5249. [CrossRef]
48. Drescher, U.; Brüggemann, D. Fluid selection for the organic Rankine cycle in biomass power and heat plants. *Appl. Therm. Eng.* **2007**, *27*, 223–238. [CrossRef]
49. HTRI Software. Available online: https://www.htri.net/about (accessed on 5 August 2023).
50. Aspen Plus. Available online: https://www.aspentech.com/en/products/engineering/aspen-plus (accessed on 5 August 2023).
51. *GB/T 151-2014*; Fouling Resistance of Industrial Fluids. National Standard of the People's Republic of China: Beijing, China, 2014; pp. 212–213.
52. Lemmon, E.W.; Huber, M.L.; McLinden, M.O. *Refprop 8.0*; NIST Standard Reference Database 23, Version 8; Informer Technologies, Inc.: Los Angeles, CA, USA, 2023.
53. Smith, R. Appendix B: Materials of Construction. In *Chemical Process Design and Integration*, 2nd ed.; John Wiley and Sons: Hoboken, NJ, USA, 2016; pp. 853–860.
54. Stainless Steel vs. Carbon Steel—Comparison—Pros and Cons. Available online: https://material-properties.org/stainless-steel-vs-carbon-steel-comparison-pros-and-cons/ (accessed on 22 October 2023).
55. Carbon Steel vs. Stainless Steel: What Is the Difference? Available online: https://www.rocheindustry.com/carbon-steel-vs-stainless-steel/#Carbon_Steel_vs_Stainless_Steel_Final_Verdict (accessed on 22 October 2023).
56. Rekkas-Ventiris, G. Archimede Concentrated Solar Power Plant Dynamic Simulation: Control Systems, Heat Transfer Fluids and Thermal Energy Storage. Master's Thesis, Politecnico di Milano, Milan, Italy, 2018.
57. Benzene Price. Available online: https://www.echemi.com/productsInformation/pid_Seven2868-benzene.html (accessed on 5 August 2023).